THE UNIVERSITY of EDINBURGH

Edinburgh Research Explorer

Synthesis and crystal structure of LiNbO3-type Mg3Al2Si3O12: A possible indicator of shock conditions of meteorites

Revision 2 (correction date April 15, 2017)

Synthesis and crystal structure of LiNbO$_3$-type Mg$_3$Al$_2$Si$_3$O$_{12}$: A possible indicator of shock conditions of

meteorites

Takayuki Ishii[1,2], Ryosuke Sinmyo[3], Tetsuya Komabayashi[4], Tiziana Boffa Ballaran[1], Takaaki Kawazoe[1],

Nobuyoshi Miyajima[1], Kei Hirose[3], Tomoo Katsura[1]

[1]Bayerisches Geoinstitut, University of Bayreuth, 95440 Bayreuth, Germany

[2]Geodynamics Research Center, Ehime University, Matsuyama, Ehime 790-8577, Japan

[3]Earth-Life Science Institute, Tokyo Institute of Technology, Meguro, Tokyo 152-8551, Japan

[4]School of GeoSciences and Centre for Science at Extreme Conditions, University of Edinburgh, Edinburgh

EH9 3FE, U.K.

Abstract

LiNbO$_3$-type Mg$_{2.98(2)}$Al$_{1.99(2)}$Si$_{3.02(2)}$O$_{12}$ (py-LN) was synthesized by recovering a run product from

2000 K and 45 GPa to ambient conditions using a large volume press. Rietveld structural refinements were

carried out using the one-dimensional synchrotron XRD pattern collected at ambient conditions. The unit-cell

lattice parameters were determined to be a = 4.8194(3) Å, c = 12.6885(8) Å, V = 255.23(3) Å^3 with Z = 6

(Hexagonal, $R3c$). The average A-O and B-O distances of the AO$_6$ and BO$_6$ octahedra have values similar to

those that can be obtained from the sum of the ionic radii of the averaged *A*- and *B*-site cations and oxygen

(2.073 and 1.833 Å, respectively). The present compound has the *B*-site cations at the octahedral site largely

shifted along the *c* axis compared with other LiNbO$_3$-type phases formed by back-transition from perovskite

(Pv)-structure, and as a result, the coordination number of this site is better described as 3 + 3. It appears

therefore that the *B*-site cation in the octahedral position cannot be completely preserved during the back-

transition because of the small size of Si and Al, which occupy usually a tetrahedral site at ambient conditions.

The formation of py-LN can be explained by the tilting of *B*O$_6$ octahedra of the perovskite structure having the

pyrope composition and formed at high *P-T* conditions. The tilting is driven by the decrease in ionic radius

ratio between the *A*-site cation and oxygen during decompression. This also explains why there is no back-

transition from the Pv-structure to the ilmenite-structure during decompression, since this is a reconstructive

phase transition whose activation energy cannot be overcome at room temperature. Py-LN may be formed in

shocked meteorites by the back-transformation after the garnet-bridgmanite transition, and will indicate shock

conditions around 45 GPa and 2000 K.

Key words: bridgmanite, large volume press, Rietveld analysis, LiNbO$_3$, high pressure

Introduction

LiNbO$_3$ (LN)-structure (space group No. 161: *R*3*c*) crystallizes in the trigonal system and is very

similar to the ilmenite (Ilm)-structure (space group: *R*$\bar{3}$), which has the same crystal system. LN- and Ilm-type

*AB*O$_3$ compounds consist of two kinds of octahedra, referred as *A*O$_6$ and *B*O$_6$ in this paper. The larger cations

are stored in the $A\mathrm{O}_6$ octahedra, whereas the smaller ones are in the $B\mathrm{O}_6$ octahedra. The two structures can be distinguished by the different arrangement of the $A\mathrm{O}_6$ and $B\mathrm{O}_6$ octahedra. The Ilm-structure has alternating layers of edge-sharing $A\mathrm{O}_6$ and $B\mathrm{O}_6$ octahedra normal to the c axis. On the other hand, each layer in the LN-structure consists of alternating edge-sharing $A\mathrm{O}_6$ and $B\mathrm{O}_6$ octahedra. The majority of LN-type $AB\mathrm{O}_3$ compounds result from the back-transformation of perovskite (Pv)-type high-pressure polymorphs during decompression. The LN-type structure is non-centrosymmetric and therefore this kind of compounds is used as functional materials of nonlinear optics and piezoelectricity. Recently, it was suggested that the degree of polarity increases with the distortion of the $B\mathrm{O}_6$ octahedra (Inaguma et al., 2012). Therefore, efforts have been made to synthesize novel LN-type compounds, sometimes by applying high-pressure techniques, and to analyze their structures. Leinenweber et al. (1991) reported that MnSnO_3 and FeTiO_3 with the Ilm-type structure transform to the Pv-type structure at high pressure and temperature, and back-transform to the LN-type structure during decompression at room temperature. They interpreted this back-transition based on the tolerance factor for the Pv-structure, t, which is defined as $t = (r_A + r_O)/\sqrt{2}(r_B + r_O)$, where r_A, r_B, and r_O are the ionic radii of the A- and B-site cations and oxygen, respectively, and concluded that Pv-structured compounds with $t < 0.84$ transform to the LN-structure by pressure release.

In the field of Earth science, various kinds of $AB\mathrm{O}_3$ compounds have been investigated as analogue materials of MgSiO_3 with the orthorhombic Pv-structure (bridgmanite, Brg), because Brg is considered to be the most abundant mineral in the Earth's lower mantle. Brg can incorporate Al^{3+} by two possible substitution mechanisms (a charge-coupled substitution (Mg + Si for 2Al) and an oxygen vacancy substitution (2Si + O for

3

2Al + one oxygen vacancy)). This incorporation shifts the stability field of Brg to higher pressures and changes its physical properties. For example, rigidity decreases and electrical conductivity increases (e.g. Kesson et al., 1995; Irifune et al., 1996; Xu et al., 1998; Walter et al., 2004; Murakami et al., 2012). It was also pointed out that the oxygen vacancy substitution may allow water incorporation (Navrotsky, 1999) although it is still unclear whether aluminous Brg can incorporate significant amounts of water. Therefore, understanding the stability and Al-substitution mechanism in Brg is one of the important subjects in Earth science.

Funamori et al. (1997) using a laser-heated diamond-anvil cell (LH-DAC) discovered that $(Mg,Fe,Ca,Mn)_3Al_2Si_3O_{12}$ natural garnet directly transforms to the Pv-structure at high pressures, and then transforms to a metastable phase with the LN-structure during decompression. Miyajima et al. (1999) examined the Pv-LN transition using natural garnets with various compositions also using a LH-DAC. These authors suggested that Brg with Al_2O_3 contents larger than 25 mol% transforms to the LN-structure during decompression. However, the structures of these LN-type compounds were not analyzed in detail because only small amount of the LN-type material was obtained together with amorphous phases, which were also formed by back-transformations in DACs. Recently, Ishii et al. (2016) succeeded in synthesizing a bulk sample of the LN-type phase with the pyrope composition $(Mg_3Al_2Si_3O_{12})$ at pressures over 40 GPa using a multi-anvil press. Since this product is almost completely composed of the LN-type phase, it is suitable for the structural analysis by the Rietveld method.

In this paper, we report the crystal structure of the LN-type $Mg_3Al_2Si_3O_{12}$ determined by X-ray powder diffraction and Rietveld analysis. The transformation mechanism of the Pv-LN back-transition and

4

implications for a possible natural occurrence of this compound are discussed.

Experimental methods

1. Sample synthesis and characterization

The $Mg_3Al_2Si_3O_{12}$ with LN-type structure was synthesized via the following three steps. Firstly, a glass with a nominal composition of $Mg_3Al_2Si_3O_{12}$ (py-glass) was produced by quenching in water a mixture of MgO, Al_2O_3 and SiO_2 with a 3:1:3 molar ratio melted at 1950 K for 1 h. The py-glass was then converted to a sintered aggregate of Ilm-type $Mg_3Al_2Si_3O_{12}$ (py-Ak) at 27 GPa and 1170 K for 1 h. The sintered py-Ak aggregate was then subjected to a press load of 15 MN and 2000 K for 3 h, quenched to ambient temperature, and then decompressed to ambient pressure. The recovered sample consisted of a sintered aggregate of LN-type $Mg_3Al_2Si_3O_{12}$ (py-LN) compound. The high P-T syntheses were conducted using a multi-anvil apparatus for ultra-high pressure generation, IRIS-15, at the Bayerisches Geoinstitut, University of Bayreuth, Germany. Details of the experimental setup are described in Ishii et al. (2016). Liu et al. (2016) reported that Brg with a pyrope composition (py-Brg) is stabilized at 45 GPa and 2000 K, and that py-LN formed by back-transition from py-Brg during decompression in a multi-anvil press installed at the BL04B1 in the synchrotron facility, Spring-8. Therefore, py-LN obtained in this study also has been likely formed by the back-transition from py-Brg during decompression from at least 45 GPa.

The phases present in the synthesis run products recovered from the second and the third final steps were identified using a laboratory micro-focused X-ray diffractometer (MF-XRD) (Bruker, D8 DISCOVER)

with a two-dimensional solid-state detector (VÅNTEC500) and a micro-focus source (IμS) of Co-Kα radiation operated at 40 kV and 500 μA. The X-ray beam was focused to 50 μm beam using a IFG polycapillary X-ray mini-lens. The run products were also examined in back-scattered electron (BSE) images by means of scanning electron microscopy (SEM) in order to determine whether minor phases were present. Compositional analysis was carried out using an electron microprobe with wavelength-dispersive spectrometers (JEOL, JXA-8200) and an accelerated voltage and probe current of 15 kV and 15 nA, respectively. Natural pyrope was used as standard material for Mg, Al and Si.

2. Synchrotron X-ray diffraction and Rietveld refinement

Angle-dispersive powder X-ray diffraction was conducted at the beam line BL10XU of the synchrotron radiation facility SPring-8, Japan. The py-LN aggregate was crushed to a powder. The powdered sample was loaded into a hole with a diameter of 300 μm in a rhenium plate with a thickness of 20 μm. X-ray beams monochromatized with a Si double monochromator were collimated to 10-20 μm in diameter to irradiate the sample. The two-dimensional diffraction patterns were collected for 1 s on a flat panel detector (PerkinElmer). The X-ray wavelength (λ = 0.41429 Å) and detector distance from the sample were calibrated using a CeO_2 standard. Five one-dimensional diffraction profiles of the sample were obtained by integrating the two-dimensional profile at different azimuth angles using the software "IPAnalyzer" (Seto et al., 2010). The five one-dimensional diffraction patterns were combined for the Rietveld refinement.

Rietveld analysis was performed using the RIETAN-FP/VENUS package (Izumi and Momma, 2007).

The VESTA software (Momma and Izumi, 2011) was used to draw crystal structures. The structure parameters of LN-type $FeTiO_3$ (Leinenweber et al., 1991) were used as an initial structure model. Unit-cell lattice parameters, scale factor, atomic coordinates and isotropic atomic displacement parameters (Table 1), and a split-type pseudo-Voigt profile fitting function formulated by Toraya (1990) were refined simultaneously. Since peaks of SiO_2 stishovite (St) were present in the synchrotron XRD, this phase was included in the Rietveld analysis, and the lattice parameters, the scale factor and the atomic coordinates were refined. A Legendre polynomial function with 12 parameters was used for fitting of the XRD background.

Results and Discussion

1. Phase identification and sample composition

The compositions of py-glass, py-Ak, and py-LN were found to be $Mg_{2.93(2)}Al_{2.00(2)}Si_{3.04(2)}O_{12}$, $Mg_{2.99(2)}Al_{2.01(2)}Si_{3.01(1)}O_{12}$, and $Mg_{2.98(2)}Al_{1.99(2)}Si_{3.02(2)}O_{12}$, respectively, in agreement with the nominal composition and confirming that the high-pressure phases have a pyrope composition.

The MF-XRD patterns of py-Ak and py-LN are shown in Fig. 1. Although both phases have similar structural features, their diffraction patterns show clear differences. For instance, the 003 peak is present in the pattern of py-Ak but it is absent in the py-LN pattern, as required by the reflections conditions of the two different space groups ($R\bar{3}$ and $R3c$, respectively) in which these two materials crystallize. All peaks can be identified as belonging to py-Ak (Fig. 1, bottom) or to py-LN (Fig. 1, top); however, some St and very small amounts of Al_2O_3 corundum (Crn) grains were identified in the BSE images taken for py-LN. The amounts of

7

these minor phases appear to be below the detection limit of the Bruker diffractometer. These trace phases may have formed during heating to 2000 K for the synthesis of py-Brg. As mentioned in the experimental session, in the synchrotron XRD pattern of py-LN, only St was present but no peaks of Crn were observed.

2. Rietveld refinement of LiNbO₃-type Mg₃Al₂Si₃O₁₂

The results of Rietveld refinements of the synchrotron XRD pattern of py-LN are shown in Fig. 2. Because the X-ray scattering factors of Mg, Al and Si atoms are very similar, it is practically impossible to determine their site occupancies at the A and B sites. Thus, these were fixed by assuming 25% of Al at each site based on the compositional analysis and complete order of Mg-Si resulting in the following occupancies: $Mg_{0.75}Al_{0.25}$ at the A site and $Si_{0.75}Al_{0.25}$ at the B site. This assumption is based on the fact that no cation disorder has been reported either for Fe-bearing, Al-free or Fe-Al-bearing bridgmanites (e.g. Horiuchi et al., 1987; Vanpeteghem et al., 2006), thus the same cation distribution is likely retained in py-LN since it is formed by the back-transformation of py-Brg. During refinement, the isotropic atomic displacement parameter (U_{iso}) of oxygen converged towards a much larger value than the one generally observed for several structures (i.e. $<\sim 0.013$ Å^2) (see Table 1). Therefore, we also performed refinements with the U_{iso} of oxygen fixed to the value obtained for LiNbO₃ by means of single-crystal structural refinement (Hsu et al., 1997). Both refinement strategies, i.e. with oxygen U_{iso} fixed or free to vary resulted in very similar crystal structures (see Table 1 and 3). In both cases, the discrepancy indexes converged to satisfactory values of less than 5% (Table 1)

The difference between the Ilm- and LN-structures can be described in terms of their c/a ratio

(Funamori et al. 1997). The ranges of c/a ratios of Ilm- and LN-type phases are 2.76-2.87 and 2.58-2.69, respectively (e.g. Ko and Prewitt, 1988; Leinenweber et al., 1991; Funamori et al., 1997; Hsu et al., 1997; Inaguma et al., 2010; Akaogi et al., 2002). The present py-LN has a c/a ratio of 2.63, which is within the range of the LN-type phases defined by Funamori et al. (1997), and is smaller than that of py-Ak reported by Akaogi et al. (2002) ($c/a = 2.80$). The unit-cell volumes and densities of the $Mg_3Al_2Si_3O_{12}$ compounds are summarized in Table 2. There is a volume increase for the py-Brg to py-LN transition at ambient conditions of ~3.0% and this value is in the range obtained for $MnTiO_3$, $MnSnO_3$, $FeTiO_3$, $ZnGeO_3$ and $MgGeO_3$ compounds (2.7-3.6%) (Leinenweber et al., 1991). The density of py-LN lies between those of py-Ak and py-Brg, which may explain the formation of py-LN and not py-Ak by back-transformation from py-Brg.

The crystal structure of py-LN is shown in Fig. 3. The bond length, bond angles, and bond valence sum (BVS) (Brown and Altermatt, 1985) and effective coordination numbers (n_c) (Hoppe, 1979) calculated from the bond lengths of the py-LN are summarized in Table 3. Neighboring AO_6 octahedra ($A = Mg_{0.75}Al_{0.25}$) and neighboring BO_6 octahedra ($B = Si_{0.75}Al_{0.25}$) are corner-sharing, whereas AO_6 and BO_6 octahedra are edge-sharing in the ab-plane and share a face along the c-axis, resulting in A-B-empty site periodicity along the c-axis (Fig. 3). The average A-O and B-O distances of the AO_6 and BO_6 octahedra are 2.033-2.043 Å and 1.840-1.843 Å, respectively. The ionic radii of Mg^{2+}, Al^{3+}, Si^{4+}, and O^{2-} in six-fold coordination are $r_{Mg} = 0.72$, $r_{Al} = 0.535$, $r_{Si} = 0.4$ and $r_O = 1.40$ Å, respectively (Shannon, 1976). The average A-O and B-O distances calculated using these ionic radii for $0.75r_{Mg} + 0.25r_{Al} + r_O$ (2.073 Å) and $0.75r_{Si} + 0.25r_{Al} + r_O$ (1.833 Å), respectively, are very similar to those obtained from the structural refinement, hence supporting the assumption of complete

order of Mg^{2+} and Si^{4+}. The BVS value of the *A* site (Table 3) is slightly larger than 2 as expected due to the Al

substitution, whereas the BVS value of the *B* site is still close to the value of 4 inspite of the presence of Al^{3+},

which has a lower valence than Si^{4+}. Moreover, the n_c value of the *B*-site cation (3.13-3.40) is much smaller

than 6 (Table 3); this derives from the large difference between the two non-equilvalent *B*-O lengths (0.427-

0.505). The *B*-site cation is largely shifted from the position at the center of the octahedron along the *c* axis,

reducing the coordination number to almost three. The n_c values of Ti^{4+} cations in LN-type $FeTiO_3$ and

$MnTiO_3$ compounds (5.0-5.2) which formed by back-transition from the corresponding Pv-type phases are

significantly larger (e.g. Ko and Prewitt, 1988; Leinenweber et al., 1991; Hsu et al. 1997). This suggests that

during the back-transformation from the py-Brg to the py-LN, the Si and Al cations tend to shift toward a

tetrahedral coordination, given that this is their preferred coordination at ambient conditions. However, a

complete reversion to such coordination is likely not possible at room temperature and the *B* site can therefore

be seen as a 3 + 3 coordination site. The large off-set of the *B* atoms from the center of the octahedra is likely

favoured by the acentric space group in which the py-LN phase crystallizes. However, additional property tests

(e.g. ferroelectric hysterisis measurement) need to be conducted to characterise the dielectric properties of py-

LN phase which likely may not present the ferroelectric behaviour of many other LN-type structures.

3. Back-transformation mechanism from py-Brg to py-LN

This study shows that the investigated compound has the LN-type structure. Liu et al. (2016) reported

that Brg with 25 mol% Al_2O_3 transforms to py-LN during decompression, whereas Brg with a lower Al_2O_3

content can be recovered. Bridgmanite has the orthorhombic perovskite structure which can be view as a result from the distortion of the cubic Pv-structure due to the too small ratio in ionic radii between the A-site cation and the 12-coordinated anion. The ionic radius of the Mg^{2+} is too small for the oxygen packing in the ideal cubic Pv-structure. Distortion to the orthorhombic symmetry decreases the actual coordination number from twelve to eight + four, which changes the AO_{12} dodecahedral site to a AO_6 prism site with two longer A-site cation-oxygen bonds (bicapped prism site) with consequent reduction of the polyhedral volume. The substition of Mg^{2+} by Al^{3+} makes the average ionic radius of the A-site cation even smaller. Accordingly, bridgmanite with pyrope composition has likely a much more distorted orthorhombic structure than pure $MgSiO_3$ bridgmanite and can be stabilized only at higher pressures, because at these conditions the relatively larger compressibility of the oxygen anions with respect to the cations favor the substitution of smaller atoms at the A site. By decreasing pressure, the oxygen atoms expand more than the A-site cations and the resulting A-site volume becomes too large for the small Mg and Al cations. This likely hinders the possibility of recovering the orthorhombic Pv-structure containing a large amount of Al (25 mol%) outside its stability field and favors the transformation to the LN-structure because of the reduction of the coordination number of the A-site cation to six.

A comparison among the orthorhombic Pv-structure ($MgSiO_3$ Brg), the LN-structure with pyrope composition and $MgSiO_3$ akimotoite is given in Figs. 4a, 4b and 4c, respectively. The Pv- and LN-structures have a very similar BO_6 octahedral framework. The transformation from the orthorhombic Pv-structure to the LN-structure is caused by the change in the tilting of the BO_6 octahedra and by the shift of the A-site cations, as

11

shown by the thick yellow and thin red arrows in Fig. 4a. These changes correspond to the transformation from the [111] cubic closed-packing layer composed of oxygen and A-site cations in the orthorhombic Pv-structure to the [001] hexagonal closed-packing layer of oxygen with an interstitial A-site cations between two oxygen layers in the LN-structure. Red balls in Figs. 4a and 4b represent the oxygen atoms coordinating the A-site cation in the Pv- and LN-structures. Due to the back-transformation, the A-site cation shifts closer to the octahedral framework giving rise to the octahedral coordination observed in the LN-structure (Fig. 4b).

The octahedral tilting can be described for the two structures in terms of B-O-B angles. These angles are all the same in the LN-structure and their value (143.0-143.3º, Table 3) is smaller than the two B-O-B angles (146.5º in the c direction and 147.0º in the b direction) of the $MgSiO_3$ Brg structure (Horiuchi et al., 1982). However, as already mentioned, the Al substitution in bridgmanite may give rise to a larger orthorhombic distortion (similar to what observed for Fe-Al-bearing bridgmanites, Vanpeteghem et al., 2006), resulting in B-O-B angles smaller than those observed for pure $MgSiO_3$ bridgmanite. It is very likely, therefore, that the Brg to LN transformation results in an increase of the B-O-B angle and hence a smaller octahedral tilting.

Py-Brg does not transform to py-Ak, but to py-LN, even though the Ilm- and LN-structures are very similar. As shown in Fig. 4c, the Ilm-structure has alternating layers of corner-sharing AO_6 and BO_6 octahedra. This arrangement cannot be obtained simply by tilting of BO_6 octahedra and displacement of the A-site cations of the Pv-structure, but requires a reconstructive transition whose activation energy cannot be overcome during the pressure release at room temperature.

12

Implication

Possible existence of py-LN in shocked meteorites

A natural LN-type $FeTiO_3$ compound was recently discovered in a shocked gneiss from the Ries Crater, Germany (e.g. Dubrovinsky et al. 2009). Akaogi et al. (2016) constrained the shock pressure needed to obtain such material in the range of 14-28 GPa, based on the stability field of Pv-type $FeTiO_3$ which likely was formed during the shocking event and then back-transformed to the LN-type $FeTiO_3$ structure after the shock relaxation. Similarly, py-LN phases might form after quenching in shocked meteorites where the pressures may rich the values needed for the transition from garnet to Brg. The recovery of such phase after a shock event depends on its thermal stability, however the py-LN phase may be also a good indicator of the formation of the Brg phase with pyrope garnet composition and can be used to constrain the *P-T* conditions of the relatively heavy shock event around 45 GPa and 2000 K at least in a similar manner as amorphous phases with the $(Mg,Fe)SiO_3$ Brg composition have been used as evidence of the formation of Brg in meteorites (Sharp et al., 1997; Tomioka and Fujino, 1997).

Acknowledgement

References cited

Akaogi, M., Abe, K., Yusa, H., Ishii, T., Tajima, T., Kojitani, H., Mori, D., and Inaguma, Y. (2016). High-pressure high-temperature phase relations in $FeTiO_3$ up to 35 GPa and 1600°C. Physics and Chemistry of Minerals, 1-11.

Akaogi, M., Tanaka, A., and Ito, E. (2002). Garnet–ilmenite–perovskite transitions in the system $Mg_4Si_4O_{12}$–$Mg_3Al_2Si_3O_{12}$ at high pressures and high temperatures: phase equilibria, calorimetry and implications for mantle structure. Physics of the Earth and Planetary Interiors, 132, 303-324.

Brown, I.D., and Altermatt, D. (1985). Bond-valence parameters obtained from a systematic analysis of the inorganic crystal structure database. Acta Crystallographica Section B: Structural Science, 41, 244-247.

Dubrovinsky, L.S., El Goresy, A., Gillet, P., Wu, X., and Simionivici, A. (2009). A Novel Natural Shock-induced High-Pressure Polymorph of $FeTiO_3$ with the Li-Niobate Structure from the Ries Crater, Germany. Meteoritics and Planetary Science Supplement, 72, 5094.

Funamori, N., Yagi, T., Miyajima, N., and Fujino, K. (1997) Transformation in garnet from orthorhombic perovskite to $LiNbO_3$ phase on release of pressure. Science, 275, 513-515.

Geiger, C.A., Newton, R.C., and Kleppa, O.J. (1987). Enthalpy of mixing of synthetic almandine-grossular and almandine-pyrope garnets from high-temperature solution calorimetry. Geochimica et Cosmochimica Acta, 51, 1755-1763.

Hoppe, R. (1979). Effective coordination numbers (ECoN) and mean fictive ionic radii (MEFIR). Zeitschrift für Kristallographie-Crystalline Materials, 150, 23-52.

Horiuchi, H., Ito, E., and Weidner, D.J. (1987) Perovskite-type $MgSiO_3$: single-crystal X-ray diffraction study. American Mineralogist, 72, 357–360.

Hsu, R., Maslen, E.N., Du Boulay, D., and Ishizawa, N. (1997) Synchrotron X-ray studies of $LiNbO_3$ and $LiTaO_3$. Acta Crystallographica Section B: Structural Science, 53, 420-428.

Inaguma, Y., Yoshida, M., Tsuchiya, T., Aimi, A., Tanaka, K., Katsumata, T., and Mori, D. (2010) High-pressure synthesis of novel lithium niobate-type oxides. In Journal of Physics: Conference Series, 215, 012131.

Inaguma, Y., Sakurai, D., Aimi, A., Yoshida, M., Katsumata, T., Mori, D., Yeon, J., and Halasyamani, P.S. (2012) Dielectric properties of a polar $ZnSnO_3$ with $LiNbO_3$-type structure. Journal of Solid State Chemistry, 195, 115-119.

Irifune, T., Koizumi, T., and Ando, J.I. (1996) An experimental study of the garnet-perovskite transformation in the system $MgSiO_3$–$Mg_3Al_2Si_3O_{12}$. Physics of the Earth and Planetary Interiors, 96, 147-157.

Ishii, T., Shi, L., Huang, R., Tsujino, N., Druzhbin, D., Myhill, R., Li, Y., Wang, L., Yamamoto, T., Miyajima, N., Kawazoe, T., Nishiyama, N., Higo, Y., Tange, Y., and Katsura, T. (2016) Generation of pressures over

40 GPa using Kawai-type multi-anvil press with tungsten carbide anvils. Review of Scientific Instruments, 87, 024501.

Izumi, F., and Momma, K. (2007) Three-dimensional visualization in powder diffraction. Solid State Phenomena, 130, 15-20.

Kesson, S.E., Gerald, J.F., Shelley, J.M.G., and Withers, R.L. (1995) Phase relations, structure and crystal chemistry of some aluminous silicate perovskites. Earth and Planetary Science Letters, 134, 187-201.

Ko, J., and Prewitt, C.T. (1988) High-pressure phase transition in $MnTiO_3$ from the ilmenite to the $LiNbO_3$ structure. Physics and Chemistry of Minerals, 15, 355-362.

Leinenweber, K., Utsumi, W., Tsuchida, Y., Yagi, T., and Kurita, K. (1991) Unquenchable high-pressure perovskite polymorphs of $MnSnO_3$ and $FeTiO_3$. Physics and Chemistry of Minerals, 18, 244-250.

Liu, Z., Irifune, T., Nishi, M., Tange, Y., Arimoto, T., and Shinmei, T. (2016) Phase relations in the system $MgSiO_3$–Al_2O_3 up to 52GPa and 2000K. Physics of the Earth and Planetary Interiors, 257, 18-27.

Miyajima, N., Fujino, K., Funamori, N., Kondo, T., and Yagi, T. (1999) Garnet-perovskite transformation under conditions of the Earth's lower mantle: an analytical transmission electron microscopy study. Physics of the Earth and Planetary Interiors, 116, 117-131.

Momma, K., and Izumi, F. (2011). VESTA 3 for three-dimensional visualization of crystal, volumetric and morphology data. Journal of Applied Crystallography, 44, 1272-1276.

Murakami, M., Ohishi, Y., Hirao, N., and Hirose, K. (2012) A perovskitic lower mantle inferred from high-pressure, high-temperature sound velocity data. Nature, 485, 90-94.

Navrotsky, A. (1999) A lesson from ceramics. Science, 284, 1788-1789.

Seto, Y., Nishio-Hamane, D., Nagai, T., and Sata, N. (2010) Development of a software suite on X-ray diffraction experiments. Review of High Pressure Science and Technology, 20(3).

Shannon, R.D. (1976) Revised effective ionic radii and systematic studies of interatomic distances in halides and chalcogenides. Acta Crystallographica, A32, 751-767.

Sharp, T.G., Lingemann, C.M., Dupas, C., and Stöffler, D. (1997) Natural occurrence of $MgSiO_3$-ilmenite and evidence for $MgSiO_3$-perovskite in a shocked L chondrite. Science, 277, 352-355.

Tomioka, N., Fujino, K. (1997) Natural $(Mg,Fe)SiO_3$-ilmenite and-perovskite in the Tenham meteorite. Science, 277, 1084-1086.

Toraya, H. (1990). Array-type universal profile function for powder pattern fitting. Journal of applied crystallography, 23, 485-491.

Vanpeteghem, C.B., Angel, R.J., Ross, N.L., Jacobsen, S.D., Dobson, D.P., Litasov, K.D., and Ohtani, E. (2006) Al, Fe substitution in the $MgSiO_3$ perovskite structure: a single-crystal X-ray diffraction study. Physics of the Earth and Planetary Interiors, 155, 96-103.

Walter, M.J., Kubo, A., Yoshino, T., Brodholt, J., Koga, K.T., and Ohishi, Y. (2004) Phase relations and equation-of-state of aluminous Mg-silicate perovskite and implications for Earth's lower mantle. Earth and Planetary Science Letters, 222, 501-516.

Xu, Y., McCammon, C., and Poe, B.T. (1998) The effect of alumina on the electrical conductivity of silicate perovskite. Science, 282, 922-924.

Figure captions

Figure 1. MF-XRD patterns of akimotoite (bottom) with the pyrope composition (py-Ak) synthesized at 27 GPa and 1170 K and LiNbO$_3$-type phase (top) also with the pyrope composition (py-LN) obtained from recovering a sample from 2000 K and 45 GPa.

Figure 2. Rietveld refinement of LiNbO$_3$-type Mg$_3$Al$_2$Si$_3$O$_{12}$. The XRD pattern was collected at atmospheric pressure and room temperature. Data points and solid lines represent the observed and the calculated profiles, respectively, and the residual curve is shown at the bottom. Bragg peak positions are shown by small ticks. The upper and lower ticks are for LiNbO$_3$-type Mg$_3$Al$_2$Si$_3$O$_{12}$ and rutile-type SiO$_2$ (stishovite), respectively.

Figure 3. Crystal structure of LiNbO$_3$-type Mg$_3$Al$_2$Si$_3$O$_{12}$ obtained using the oxygen-U_{iso}-fixed model (note that this structure is identical to that obtained from the oxygen-U_{iso}-free model). The solid line is the unit-cell. Occupancies of Mg and Al at the *A* site and Si and Al at the *B* site are shown with areas of different colors in each sphere. Smaller spheres are oxygen. BVS and n_c represent the bond valence sum values and effective coordination numbers of each site, respectively (Table 3).

Figure 4. Structural relationship among (a) orthorhombic Pv-type MgSiO$_3$ (Brg), (b) LN-type Mg$_3$Al$_2$Si$_3$O$_{12}$ (py-LN) and (c) Ilm-type MgSiO$_3$ (Ak). Thick yellow and thin red arrows indicate the tilting directions of the octahedra and the shifting directions of the *A*-site cations during the Brg to LN transition, respectively. The structure of Brg is viewed down the *a* direction, whereas, for comparison, py-LN and Ak are viewed in the

18

$[1\bar{1}2]_{hex}$ and $[012]_{hex}$ plane. Red balls represent the oxygen atoms bonded to the *A*-site cations in Brg and py-LN.

The two dashed white lines in Brg represent the two longer *A*-site cation-oxygen bonds of the AO_8 polyhedron.

AO_6 and BO_6 octahedra are shown for Ak. Dashed lines in Ak indicate the directions of the alternating AO_6 and

BO_6 layers.

Table 1. Structural parameters of LiNbO₃ (LN)-type $Mg_{2.98(2)}Al_{1.99(2)}Si_{3.02(2)}O_{12}$ refined in space group $R3c$ (No. 161)

Site	Wyckoff site	g(Mg or Si)	g(Al)	x	y	z	U_{iso} (Å²)
A[a]	6a	0.75[b]	0.25[b]	0	0	0	0.0089(7)
		0.75[b]	0.25[b]	0	0	0	0.0160(8)
B[a]	6a	0.75[b]	0.25[b]	0	0	0.2154(1)	0.0038(8)
		0.75[b]	0.25[b]	0	0	0.2145(1)	0.0113(9)
O	18b	-	-	0.3473(5)	0.0681(4)	0.1035(3)	0.0067[c]
		-	-	0.3430(5)	0.0613(4)	0.1060(3)	0.0242(8)

For each atom the values obtained from the oxygen-U_{iso}-fixed refinements are reported in the upper lines, whereas those obtained from the oxygen-U_{iso}-free refinements are reported in the lower line.

For the oxygen-U_{iso}-fixed refinements we obtained unit-cell lattice parameters: a = 4.8194(3) Å, c = 12.6885(8) Å, V = 255.23(3) Å³, Z = 6, V_m (molar volume) = 25.617(3) cm³/mol and D = 3.934(1) g/cm³.

Discrepancy factors: R_{wp} = 4.108%, R_e = 3.253%

LN phase: R_B = 1.188%, R_F = 0.506%

SiO₂ stishovite: R_B = 1.420%, R_F = 1.020%

For the oxygen-U_{iso}-free refinements we obtained unit-cell lattice parameters: a = 4.8194(3) Å, c = 12.6887(8) Å, V = 255.24(3) Å³, Z = 6, V_m = 25.618(5) cm³/mol and D = 3.934(1) g/cm³.

Discrepancy factors: R_{wp} = 3.615%, R_e = 3.255%

LN phase: $R_B = 0.838\%$, $R_F = 0.396\%$

SiO$_2$ stishovite: $R_B = 3.693\%$, $R_F = 1.274\%$

$$R_{wp} = \left\{\frac{\sum_i w_i [y_i - f_i(x)]^2}{\sum_i w_i y_i^2}\right\}^{1/2}, \quad R_B = \frac{\sum_K |I_0(\boldsymbol{h}_K) - I(\boldsymbol{h}_K)|}{\sum_K I_0(\boldsymbol{h}_K)}, \quad R_F = \frac{\sum_K ||F_0(\boldsymbol{h}_K)| - |F(\boldsymbol{h}_K)||}{\sum_K |F_0(\boldsymbol{h}_K)|}, \quad R_e = \left\{\frac{N-P}{\sum_i w_i y_i^2}\right\}^{1/2}$$

where y_i, w_i and $f_i(x)$ are the intensity observed at step i, the statistical weight and theory intensity, respectively.

$I_0(\boldsymbol{h}_K)$, $I(\boldsymbol{h}_K)$, $F_0(\boldsymbol{h}_K)$ and $F(\boldsymbol{h}_K)$ are the observed and calculated intensities and structure factors for reflection K, respectively. N and P are number of all data points and refined parameters, respectively.

$g(M)$: site occupancy of M.

[a]A and B atom positions are occupied by Mg or Al and Si or Al, respectively.

[b]Site occupancies are fixed.

[c]Isotropic atom displacement parameter of oxygen is fixed to that of LiNbO$_3$ reported by Hsu et al. (1997).

Table 2. Volumes and densities of $Mg_3Al_2Si_3O_{12}$ compounds.

	V_m (cm^3/mol)	V (Å^3/formula unit)	D (g/cm^3)	Reference
Pyrope	113.13(3)	46.959(3)	3.564(1)	Geiger et al. (1987)
py-Ak	104.63(5)	43.437(5)	3.853(1)	Akaogi et al. (2002)
py-LN	102.47(5)	42.538(5)	3.934(1)	This study
py-Brg[a]	99.5(7)	41.3(7)	4.06(3)	Liu et al. (2016)

Py-Ak, py-LN and py-Brg represent ilmenite, $LiNbO_3$ and perovskite phases with pyrope composition, repectively.

[a]Unit-cell lattice parameters of Brg with Al_2O_3 content ($\sim$29$\pm$5 mol%) from Liu et al. (2016).

Table 3. Interatomic distances and angles of LiNbO$_3$-type Mg$_{2.98(2)}$Al$_{1.99(2)}$Si$_{3.02(2)}$O$_{12}$.

Bond length (Å)

A−O^i × 3	2.021(3)	B−O^{iii} × 3	1.587(2)
	2.031(3)		1.629(3)
A−O^{ii} × 3	2.064(2)	B−O^{vi} × 3	2.092(2)
	2.035(3)		2.056(3)
Average	2.043	Average	1.840
	2.033		1.843
BVS (A)	2.27	BVS (B)	4.23
	2.33		3.96
		^{IV}BVS (B)^a	3.66
			3.33
$n_{c, A}$	5.98	$n_{c, B}$	3.13
	6.00		3.40

Bond angles (°)

O^i−A−O^{iii}	82.3(1)	O^{ii}−A−O^{iv}	105.9(1)	O−A−O^v	160.8(2)
	82.1(1)		106.5(1)		159.6(2)
O^{vi}−B−O^{vii}	102.3(2)	O−B−O^i	89.0(1)	O−B−O^{iii}	163.2(2)

	101.0(2)		89.07(6)		164.9(2)
A–O–B^{v}	103.7(2)	A–O–B	83.27(1)	A–O^{viii}–B^{v}	86.6(1)
	101.5(2)		83.40(8)		83.41(8)
A–O^{vii}–A^{ix}	117.6(1)	B–O^{vii}–B^{vii}	143.3(1)		
	118.5(1)		143.0(2)		

Symmetry codes: (i) $-y$, $x-y$, z. (ii) $-x+y+2/3$, $y+1/3$. (iii) $-x+y$, $-x$, z. (iv) $x+2/3$, $x-y+1/3$, $z+5/6$. (v) $-y+2/3$, $-x+1/3$, $z+5/6$. (vi) $x+1/3$, $x-y+2/3$, $z+1/6$. (vii) $-y+1/3$, $-x+2/3$, $z+1/6$. (viii) $-x+y+2/3$, $y+1/3$, $z+5/6$. (ix) $x+2/3$, $y+1/3$, $z+1/3$.

The upper and lower lines reported for each site represent the oxygen-U_{iso}-fixed and oxygen-U_{iso}-free refinements, respectively.

BVS: bond valence sum value

n_c: effective coordination number

[a]^{IV}BVS (B) represents the value calculated with three shorter and one longer oxygen-B cation bond lengths.
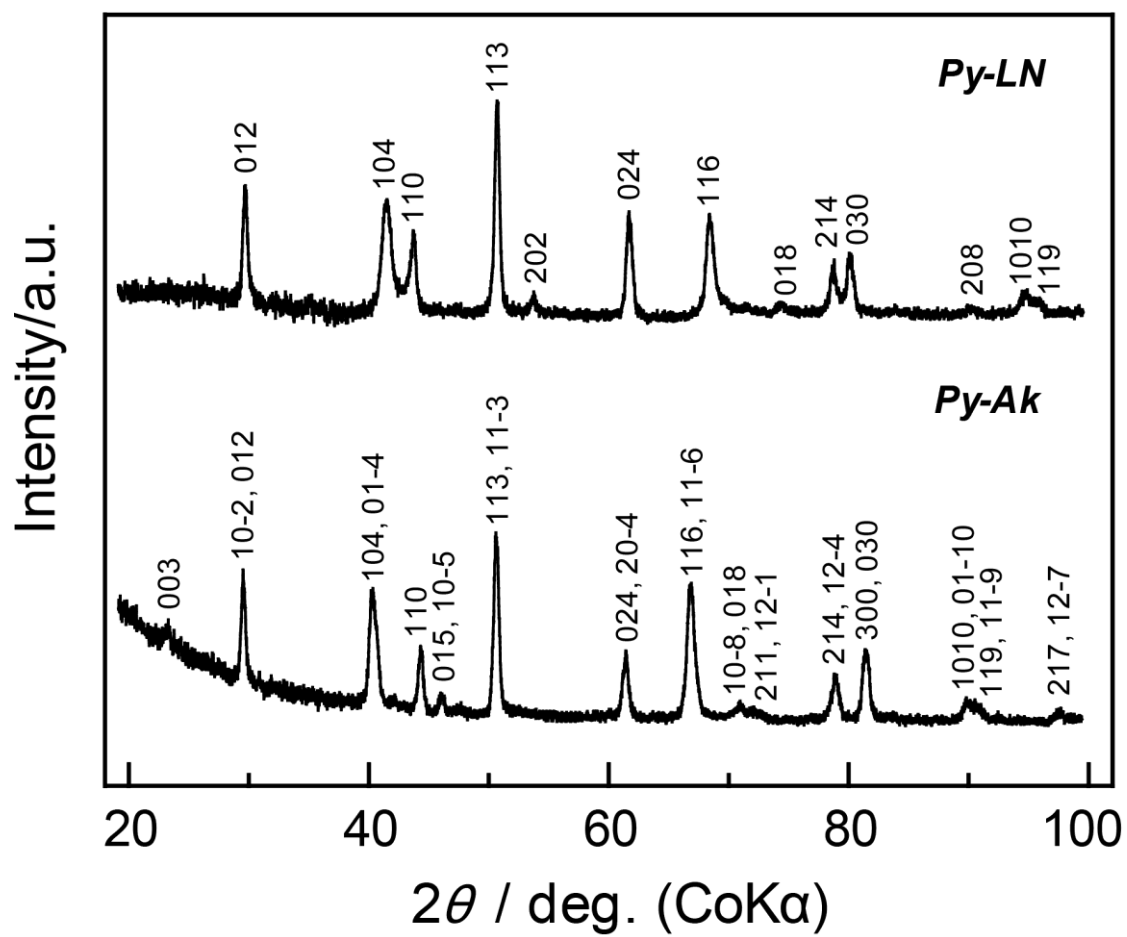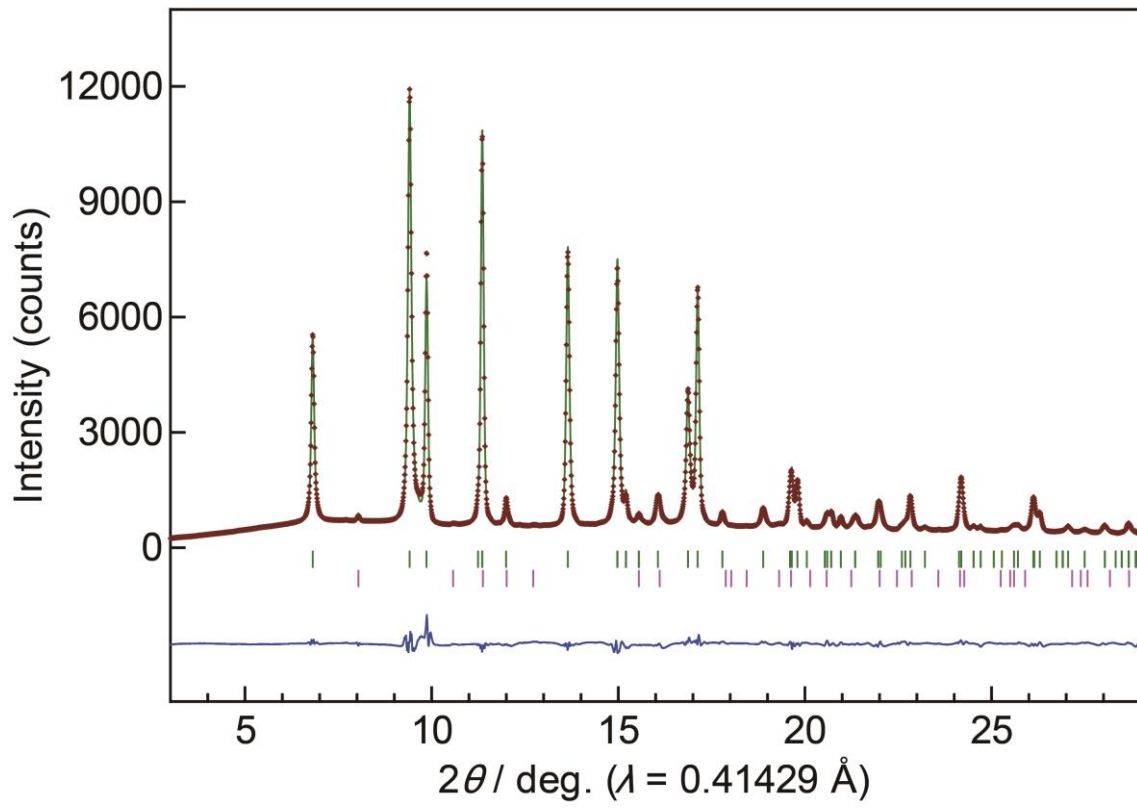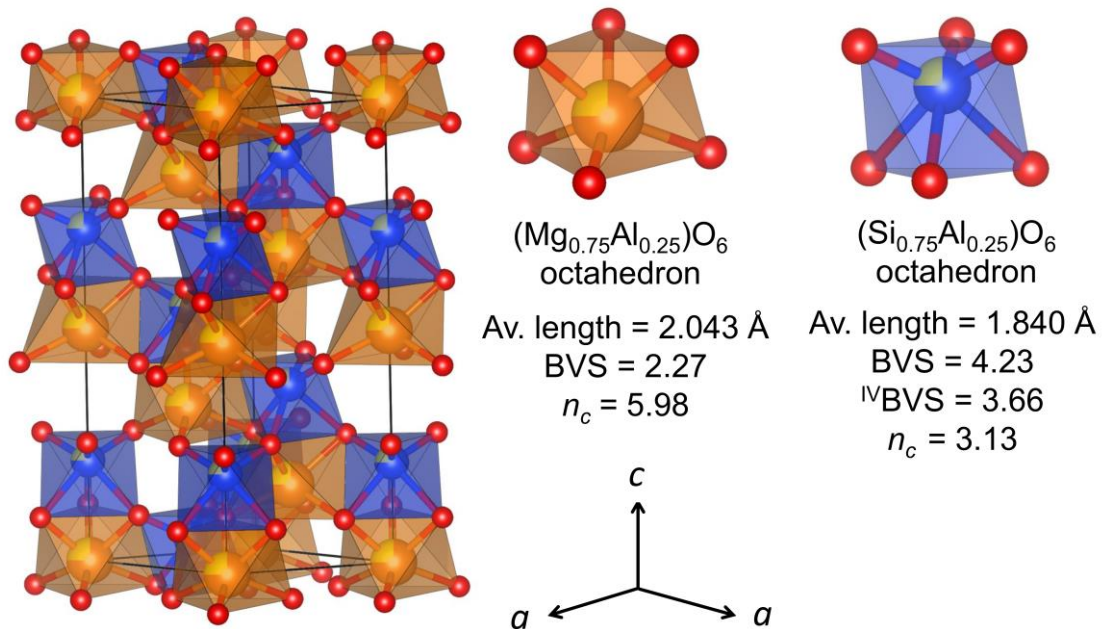
Fig. 1

Fig. 2

Fig. 3

(Mg$_{0.75}$Al$_{0.25}$)O$_6$
octahedron

Av. length = 2.043 Å
BVS = 2.27
n_c = 5.98

(Si$_{0.75}$Al$_{0.25}$)O$_6$
octahedron

Av. length = 1.840 Å
BVS = 4.23
^{IV}BVS = 3.66
n_c = 3.13

Fig. 4

(a) Brg (*Pbnm*) (b) Py-LN (*R*3*c*) (c) Ak (*R*$\bar{3}$)

AO_6 octahedron

BO_6 octahedron

a

b

c

b

$[012]_{hex}$

$[1\bar{1}2]_{hex}$

AO_6 layer

BO_6 layer

A-site cation

B-site cation